



# Materials and processing approaches for foundry-compatible transient electronics

Jan-Kai Chang<sup>a,b,1</sup>, Hui Fang<sup>c,1</sup>, Christopher A. Bower<sup>d</sup>, Enming Song<sup>a,e</sup>, Xinge Yu<sup>a,b</sup>, and John A. Rogers<sup>a,b,f,g,h,i,j,k,l,m,n,2</sup>

<sup>a</sup>Department of Materials Science and Engineering, University of Illinois at Urbana–Champaign, Urbana, IL 61801; <sup>b</sup>Frederick Seitz Materials Research Laboratory, University of Illinois at Urbana–Champaign, Urbana, IL 61801; <sup>c</sup>Department of Electrical and Computer Engineering, Northeastern University, Boston, MA 02115; <sup>d</sup>X-Celeprint, Inc., Durham, NC 27709; <sup>e</sup>Department of Materials Science, Fudan University, Shanghai 200433, People's Republic of China; <sup>f</sup>Department of Materials Science and Engineering, Northwestern University, Evanston, IL 60208; <sup>g</sup>Department of Biomedical Engineering, Northwestern University, Evanston, IL 60208; <sup>h</sup>Department of Neurological Surgery, Northwestern University, Evanston, IL 60208; <sup>i</sup>Department of Chemistry, Northwestern University, Evanston, IL 60208; <sup>j</sup>Department of Mechanical Engineering, Northwestern University, Evanston, IL 60208; <sup>k</sup>Department of Electrical Engineering and Computer Science, Northwestern University, Evanston, IL 60208; <sup>l</sup>Simpson Querrey Institute, Northwestern University, Evanston, IL 60208; <sup>m</sup>Feinberg School of Medicine, Northwestern University, Evanston, IL 60208; and <sup>n</sup>Center for Bio-Integrated Electronics, Northwestern University, Evanston, IL 60208

Contributed by John A. Rogers, June 2, 2017 (sent for review May 11, 2017; reviewed by Martin Kaltenbrunner, Michael C. McAlpine, and Bozhi Tian)

**Foundry-based routes to transient silicon electronic devices have the potential to serve as the manufacturing basis for “green” electronic devices, biodegradable implants, hardware secure data storage systems, and unrecoverable remote devices. This article introduces materials and processing approaches that enable state-of-the-art silicon complementary metal-oxide-semiconductor (CMOS) foundries to be leveraged for high-performance, water-soluble forms of electronics. The key elements are (i) collections of biodegradable electronic materials (e.g., silicon, tungsten, silicon nitride, silicon dioxide) and device architectures that are compatible with manufacturing procedures currently used in the integrated circuit industry, (ii) release schemes and transfer printing methods for integration of multiple ultrathin components formed in this way onto biodegradable polymer substrates, and (iii) planarization and metallization techniques to yield interconnected and fully functional systems. Various CMOS devices and circuit elements created in this fashion and detailed measurements of their electrical characteristics highlight the capabilities. Accelerated dissolution studies in aqueous environments reveal the chemical kinetics associated with the underlying transient behaviors. The results demonstrate the technical feasibility for using foundry-based routes to sophisticated forms of transient electronic devices, with functional capabilities and cost structures that could support diverse applications in the biomedical, military, industrial, and consumer industries.**

soft electronics | biodegradable electronics | transfer printing | undercut etching | hydrolysis

Semiconductor technology is increasingly essential to nearly all aspects of modern society, with projections of market sizes that will exceed \$7 trillion in 2017, equivalent to 10% of the world's gross domestic product (1–4). The rapid and accelerating pace of innovation in this area leads to increases in the frequency with which consumers upgrade their devices, thereby contributing to the production of >50 million tons of electronic waste (e-waste) each year (5, 6). Furthermore, the anticipated emergence of electronics for internet-of-things applications, along with the continued proliferation of radio frequency (RF) identification tags and other high-volume electronic goods, create daunting challenges with the management of this e-waste (7, 8). These considerations motivate research into forms of electronics that can degrade naturally into the environment to harmless end products. Such technology is also of interest for other, unique classes of applications, ranging from biodegradable, temporary electronic implants to hardware secure data systems and unrecoverable, field-deployed devices (9–12). Sometimes referred to collectively as transient electronics, these types of devices can be constructed by using designer materials, such as specially formulated polymers or natural products (13–16), or clever combinations of established materials, well-aligned to existing infrastructure (e.g., device designs, circuit topologies, manufacturing

capabilities) in conventional, nontransient electronics (17–19). The latter approach is particularly attractive due to recent research findings that establish many options in high-quality electronic materials for this purpose, ranging from semiconductor-grade monocrystalline silicon (hydrolysis to hydrogen gas and silicic acid) to dissolvable metals (e.g., Mg, W, Mo) and water-soluble dielectrics (e.g., MgO, SiO<sub>2</sub>, Si<sub>3</sub>N<sub>4</sub>) (19–23). Carefully selected device designs and encapsulation layers allow electronic systems formed with these materials to operate in a stable, high-performance manner for a desired time and then to degrade and disappear completely, at a molecular level, to biocompatible and ecofriendly end products. The results enable bioresorbable implants that bypass secondary surgical procedures for extraction, environmental sensors that avoid the need for retrieval and collection after use, and compostable electronics that eliminate costs and risks associated with recycling operations (24–26). Specific examples in the research literature include simple passive and active components (e.g., resistors, Si transistors), complementary metal-oxide-semiconductor (CMOS) inverters and their logic gates, sensors and detectors, energy storage devices and harvesters, and wireless RF power scavengers (27–30). The most recent results show, in fact, that transient electronics can be built using conventional tools in a CMOS fabrication environment, with device and circuit designs that incorporate biodegradable materials, such as Si, SiO<sub>2</sub>, and W, with only minute amounts of nondegradable materials, such as

## Significance

**Bioresorbable electronic systems have the potential to create important new categories of technologies, ranging from temporary biomedical implants to environmentally benign, green consumer devices. The results presented here provide a collection of ideas that establish the foundations for a realistic technology of this type, in which state-of-the-art silicon complementary metal-oxide-semiconductor foundries serve as the source of microscale, water-soluble electronic components configured for rapid assembly and electrical interconnection on soft, biocompatible polymer substrates. Demonstrations in various high-performance electronic systems illustrate the concepts, and fundamental studies establish the chemical kinetics and end products of dissolution in aqueous environments.**

Author contributions: J.-K.C., H.F., C.A.B., and J.A.R. designed research; J.-K.C. and E.S. performed research; J.-K.C., X.Y., and J.A.R. analyzed data; and J.-K.C. and J.A.R. wrote the paper.

Reviewers: M.K., Johannes Kepler University; M.C.M., University of Minnesota; and B.T., The University of Chicago.

The authors declare no conflict of interest.

Freely available online through the PNAS open access option.

<sup>1</sup>J.-K.C. and H.F. contributed equally to this work.

<sup>2</sup>To whom correspondence should be addressed. Email: jrogers@illinois.edu.

Ti/TiN (19). Tungsten is known to be biologically functional and its effects on the environment are minimal. Both Ti and W are used in medical implants (31, 32). These advances are critically important to the development of transient electronics into a widespread technology, where high-volume, low-cost production capabilities in existing industrial manufacturing facilities combine with methods in integration on biodegradable substrates and schemes in fabrication of metal interconnects and encapsulation layers.

Any such approach requires separation of functional elements formed on the near-surface regions of semiconductor wafers from the bulk underlying material. Early work in flexible, non-transient electronics established strategies for releasing thin Si CMOS components by anisotropic etching of Si wafers with (111) orientation or by removing the buried oxide (BOX) layers of silicon on insulator substrates (33–35). The need for specialized wafers and aggressive etchants represents a drawback of these approaches. Alternatively, wafer grinding can eliminate most of the wafer material, but efforts to design commercially relevant manufacturing schemes based on this approach have been unsuccessful (36). Here, we introduce materials and release strategies that allow foundry-produced components and integrated circuits to be rendered in eco- and biodegradable forms on polymeric substrates. The process uses conventional silicon on insulator (SOI) substrates [i.e., Si (100) handle wafers] with a fabrication sequence and design toolkit that exist as commercially accessible options at large CMOS foundries. Results include demonstrations with a range of high-performance silicon devices sourced from a commercial foundry and studies of the dissolution processes in phosphate buffer solution (PBS).

## Results and Discussion

Formation of biodegradable silicon electronic systems starts with controlled release of fully formed circuits and/or circuit components by anisotropic wet chemical etching, followed by assembly/integration onto a target substrate via transfer printing. The process reported here involves commercial chips based on the XI10 technology available from X-FAB Semiconductor Foundries, which uses 1- $\mu\text{m}$  design rules in a partially depleted SOI CMOS process originally designed for applications that demand stable operation at high temperatures (37, 38). Completed 6-inch wafers, as shown in Fig. 1A, include a Si device layer (250 nm thick) and a BOX layer (1  $\mu\text{m}$  thick), with interlayer dielectric (ILD; 750 nm thick) and intermetal dielectric (IMD; 650 nm thick) layers of  $\text{SiO}_2$  with up to three layers of metal interconnects and via plugs of W (300 nm thick, with 100-nm-thick Ti/TiN adhesion layers). Fig. 1 shows a schematic illustration, an optical micrograph, and scanning electron microscopy (SEM) images of a representative array of devices, including capacitors, p-channel and n-channel transistors, undercut-etched from the (100) silicon handle wafer (500  $\mu\text{m}$  thick). As illustrated in Fig. 1C, the procedure for release from the underlying substrate exploits lithographically defined structures and anisotropic wet chemical etching, with the BOX as a back-surface etch stop. First, patterned etching of the ILD and IMD layers creates isolated regions around individual devices that serve as building blocks for the transient electronic systems. Deposition of a layer of  $\text{SiN}_x$  ( $\approx 600$  nm) with low stress by plasma-enhanced chemical-vapor deposition (PECVD) at 300  $^\circ\text{C}$  forms a uniform encapsulation/carrier layer across the entire wafer. Next, inductively coupled

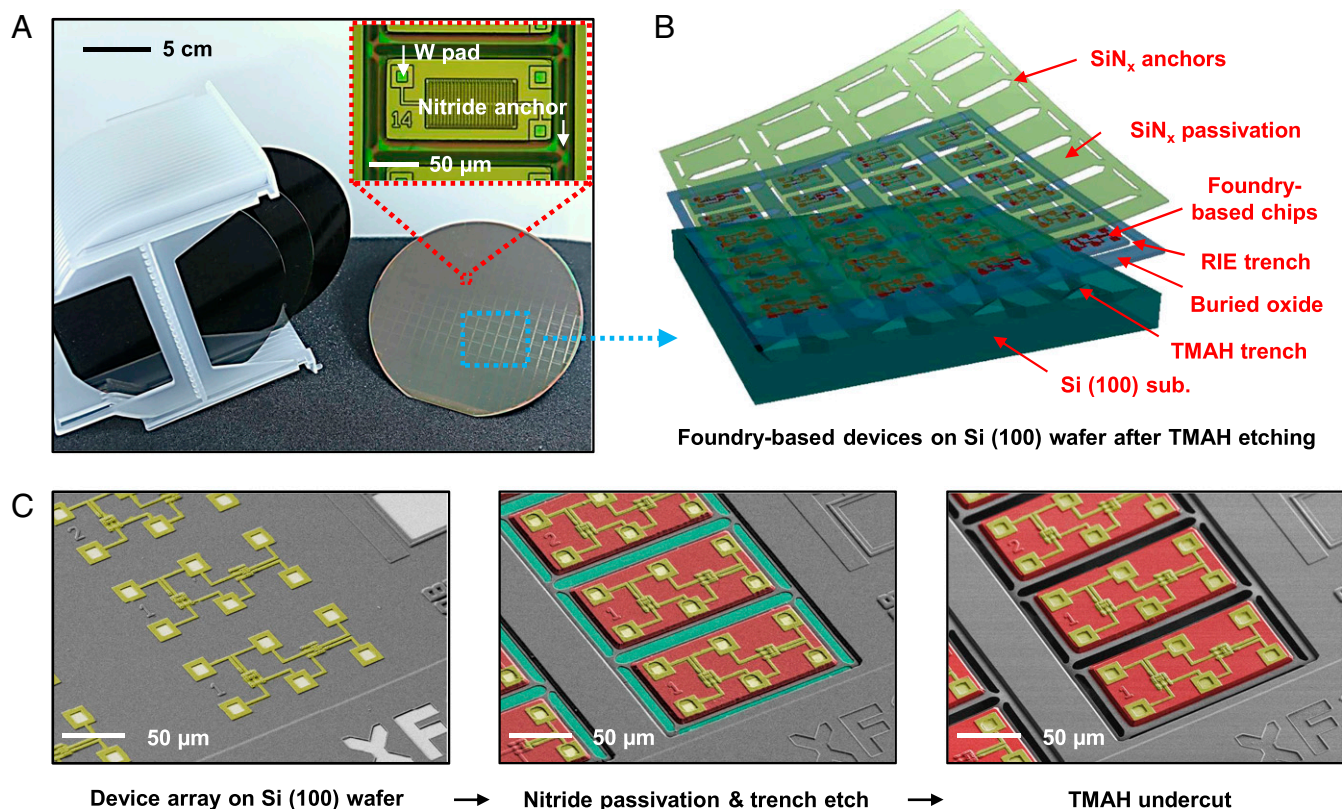


**Fig. 1.** Wafer-scale release of foundry-based, ultrathin silicon components for transient electronics. (A) Photograph of fully processed wafers. (Inset) Magnified view that shows the releasable configuration of a representative device in this foundry-based platform. (B) Schematic illustration of such device arrays after undercut release by TMAH anisotropic etching. (C) SEM images of key processing steps for release. The colorized regions correspond to the device array (gold), the released region of individual device blocks (red), and the underlying silicon (100) handle wafer (cyan). The individual frames correspond to the unprocessed wafer (Left), the wafer after passivation and trench etching (Center), and the wafer after TMAH undercut etching (Right), respectively.



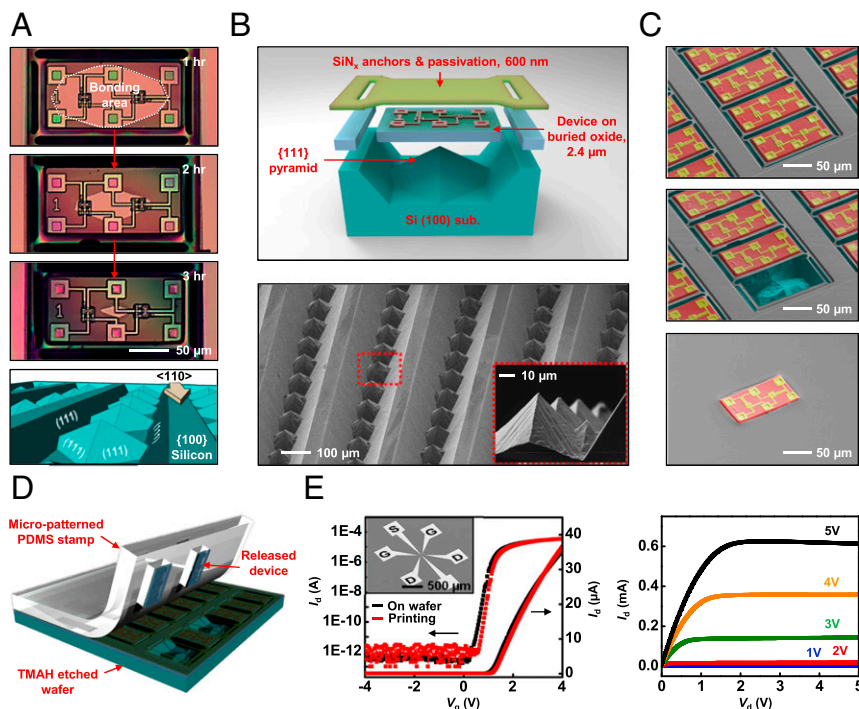
plasma (ICP) reactive ion etching (RIE) through the BOX to the handle wafer establishes trenches between the device blocks for undercut etching. Lithographically patterned tethers, or anchors, join each corner across the trenches of the exposed silicon handle. Immersing the resulting chips in baths of potassium hydroxide (KOH; 18 wt% at 70 °C) or tetramethylammonium hydroxide (TMAH, 8.3 wt% at 85 °C) leads to anisotropic etching of the underlying (100) silicon. The SiN<sub>x</sub> on the top side and the BOX on the bottom side protect the device blocks from these etchants. The result is a collection of free-standing blocks tethered to their original locations on the wafer by nitride anchors at the corners.

To facilitate release, the orientation of the devices is such that their edges are parallel to the wafer flat (i.e., Si <110>). Here, trench openings created by ICP-RIE along the Si <110> direction allow rapid removal [100-fold faster than Si (111)] of exposed silicon in the Si (110) and Si (100) planes, thereby laterally etching the wafer to undercut the devices. The micrographs in Fig. 2 show a representative device at various stages of undercut with TMAH. The thin geometries ( $\approx 3 \mu\text{m}$ , including the nitride passivation, active device structures, and BOX layer) and the properties of the constituent materials provide sufficient levels of optical transparency to allow direct visualization of regions that remain connected to the underlying silicon wafer (Fig. 2A). As a result, monitoring the progression of the undercut can be performed easily by visible microscope inspection. Careful control, combined with optimized procedures for transfer printing, can lead to cumulative yields of greater than 99%. Schematic illustrations and SEM images of the undercut profiles appear in Fig. 2B. The results are consistent with etching that proceeds in the

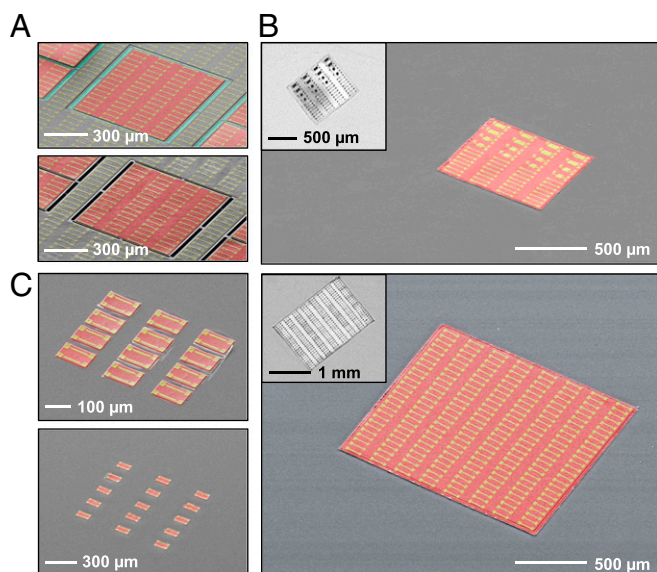
Si <110> direction, bounded by (111) planes. By consequence, an undercut process that begins at the RIE trenches leaves {111} silicon pyramids positioned at the centers of the device blocks (39).

Fig. 2C shows SEM images of representative devices in sequence from suspension above the handle wafer to removal and delivery onto a foreign substrate by transfer printing. The BOX serves as an integrated encapsulation layer on the backsides of the devices. The top coating of PECVD SiN<sub>x</sub> provides not only a passivation layer that isolates the devices from the etching baths but also a strain-compensating layer that reduces bowing of the devices after their release. The transfer printing process uses stamps of poly(dimethylsiloxane) (PDMS) with relief features defined to manipulate one device at a time or large collections of them simultaneously. A schematic representation of this process appears in Fig. 2D. The transfer and output characteristics of typical n-channel metal-oxide-semiconductor field-effect transistors (MOSFETs) processed in this manner are consistent with expected performance [on/off ratio of  $\approx 10^8$ , subthreshold slope of  $\approx 100 \text{ mV}\cdot\text{decade}^{-1}$ , on-resistance of  $\approx 18 \text{ k}\Omega$  at gate voltage ( $V_g$ ) = 5 V] as shown in Fig. 2E.

This transfer scheme is compatible with a wide range of sizes and shapes of the device blocks, their distributions across the source wafer, and numbers of them that are manipulated in each cycle of the process. By comparison with traditional pick/place tools, transfer printing is effective with far smaller and thinner devices, and at much higher throughputs. A repetitive sequence of transfer operations can distribute devices over areas on a target substrate that are much larger than those areas defined by the source wafers (40). Certain applications require large numbers of small devices in arrays, as shown in Fig. 3B; others demand only



**Fig. 2.** Aspects of release of thin, transient CMOS devices based on anisotropic etching of the Si (100) handle wafer. (A, Top) Optical micrographs collected at 1 h, 2 h, and 3 h after undercut etching to release a representative device (n-channel MOSFET). (A, Bottom) Schematic illustration of the anisotropic etching profile associated with the Si (100) substrate. (B, Top) Schematic exploded view illustration of the structural configuration of a unit cell in an array of devices after complete release. The etched areas are bounded by Si (111) planes, with freely suspended devices tethered by SiN<sub>x</sub> anchors across the trenches. (B, Bottom) SEM images of etched structures in the Si (100) handle wafer after removal of the released devices. (C) SEM images of an array of devices (colorized using a scheme similar to the scheme in Fig. 1 for ease of viewing), shown in sequence, after undercut etching (Top), after removal of a single device from the handle wafer (Middle), and after transfer printing of this device onto a target substrate (Bottom). (D) Schematic illustration of the process for transfer printing with a PDMS stamp. (E, Left) Linear and log-scale transfer characteristics of an n-channel MOSFET before (black) and after (red) transfer. (E, Right) Output characteristics of the same transistor.  $I_d$ , drain current;  $V_g$ , gate voltage.



**Fig. 3.** Released and transfer printed arrays of thin, foundry-based transient electronic devices of various sizes at different area coverages and spatial distributions. (A) SEM images of a  $4 \times 16$  array of diodes before (Top) and after (Bottom) undercut releasing. (B) SEM images of dense (Top, with pitch of  $80 \mu\text{m}$  and  $10 \mu\text{m}$ ) and sparse (Bottom, with pitch of  $250 \mu\text{m}$  and  $100 \mu\text{m}$ ) collections of device blocks on thin sheets of PLGA, illustrating the scalability of area expansion. (C) SEM images of devices with dimensions of  $\sim 0.8 \times 1 \text{ mm}^2$  (Top) and  $\sim 1.5 \times 2 \text{ mm}^2$  (Bottom) printed onto PLGA. (Insets) Optical micrographs. These images are colorized for ease of viewing (cyan, silicon handle wafer; gold, device array; red, released region of foundry-based chips).

single chips with relatively large lateral dimensions. Fig. 3 shows an example of the latter, in which the devices have dimensions of  $0.8 \times 1 \text{ mm}^2$  and  $1.5 \times 2 \text{ mm}^2$  (Fig. 3C).

Transferred devices can be interconnected by patterned thin layers of W. The bioresorbable copolymer poly(lactic-coglycolic acid) (PLGA) serves as a transient substrate and planarization layer in the examples in Fig. 4A, where a pair of n-channel and p-channel MOSFETs [channel width ( $W$ ) =  $6 \mu\text{m}$ , channel length ( $L_{\text{ch}}$ ) =  $1.8 \mu\text{m}$  for n-channel MOSFETs,  $L_{\text{ch}}$  =  $1 \mu\text{m}$  for p-channel MOSFETs] yields CMOS logic gates. The posttransfer

process begins with application of a planarizing coating of PLGA, using an anisole-based solution to prevent printed devices from washing away during the spin-coating process. This solvent is attractive because its high volatility minimizes dissolution of the PLGA substrate. The resulting coating conforms to the step edges at the perimeters of the devices ( $\approx 3 \mu\text{m}$  in height) to facilitate formation of interconnects over these features. Plasma etching through a photolithographically patterned hard mask of Mg ( $100 \text{ nm}$ ) creates openings through the PLGA at the positions of the contact pads on the device blocks. The positively sloped sidewalls that result from this etching process facilitate continuous metal interconnects patterned by photolithography and etching. Fig. 4B shows output voltage characteristics for a CMOS inverter (Left), a negative-AND (NAND) (Middle), and a negative-OR (NOR) (Right) circuit obtained in this manner. For the inverter, the voltage transfer characteristics exhibit gains of up to  $\approx 21$  at supply bias levels of  $\pm 3 \text{ V}$ , with input low voltage ( $V_{\text{IL}}$ ) of  $0.05 \text{ V}$  and input high voltage ( $V_{\text{IH}}$ ) of  $0.85 \text{ V}$ , capable of a large noise margin for high noise immunity. For the NAND and NOR gates, the output voltages below  $0.1 \text{ V}$  and over  $2.8 \text{ V}$  are considered as a logic low (0) state and a logic high (1) state, respectively, with the input voltages,  $V_A$  and  $V_B$ , switching between  $0 \text{ V}$  (for the 0 state) and  $3 \text{ V}$  (for the 1 state) to drive particular functions for the logic gates.

The resulting systems are mechanically flexible by virtue of their small thicknesses and the bendability of the PLGA substrates, as exemplified in Fig. 5A. Bending into cylinders with various diameters reveals invariant operating properties for radii of curvature as small as a few millimeters (Fig. 5B). Specifically, electrical measurements on n-channel MOSFETs at such curvatures indicate on/off ratios of  $>10^7$ , with mobilities from  $610$  to  $680 \text{ cm}^2 \cdot \text{V}^{-1}$ . The observed systematic variations likely arise from bending-induced strains in the channel and associated changes in charge carrier mobilities. With the simple approximation that the bending strain is  $\epsilon_x = t/2/R$ , where  $x$  is parallel to the channel length in the Si  $\langle 110 \rangle$  direction,  $R$  is the bending radius, and  $t$  is the thickness of the flexible electronic systems, the expected mobility enhancement,  $\Delta\mu_e/\mu_e$ , is  $\sim 1.5\%$  (for  $R = 5 \text{ mm}$ ),  $\sim 4.2\%$  (for  $R = 2.5 \text{ mm}$ ), and  $\sim 7.7\%$  (for  $R = 1.5 \text{ mm}$ ) under the induced uniaxial tensile strain and at an effective field of  $0.4 \text{ MV} \cdot \text{cm}^{-1}$  (41, 42). The data indicate device mobilities of  $624 \text{ cm}^2 \cdot \text{V}^{-1}$  (for planar),  $618 \text{ cm}^2 \cdot \text{V}^{-1}$  (for  $R = 5 \text{ mm}$ ),  $657 \text{ cm}^2 \cdot \text{V}^{-1}$  (for  $R = 2.5 \text{ mm}$ ), and  $677 \text{ cm}^2 \cdot \text{V}^{-1}$  (for  $R = 1.5 \text{ mm}$ ) that are qualitatively consistent

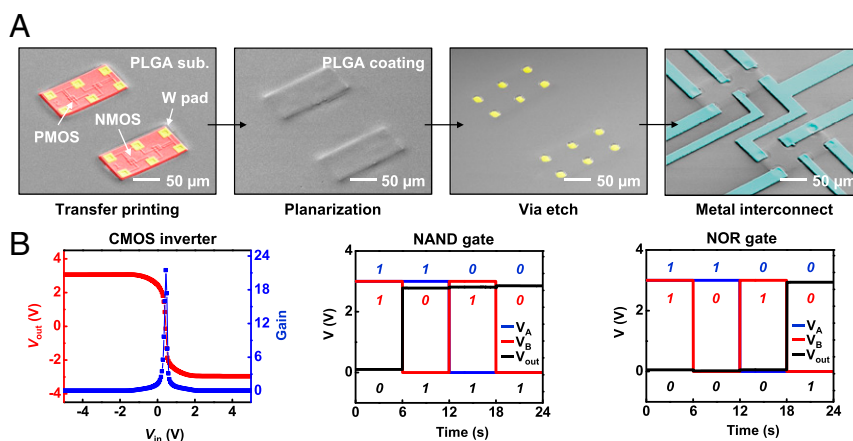


**Fig. 4.** Microscale assembly/integration of foundry-based transient CMOS devices on PLGA substrates. (A) Sequence of SEM images to illustrate the process for forming interconnects to a representative pair of n-channel and p-channel MOSFETs. The colorized regions correspond to original contact pads (yellow), individual device units (red), and interconnect leads (blue). (B) Output voltage characteristics of a CMOS inverter (Left), a NAND gate (Center), and a NOR gate (Right). The supply voltage is  $3 \text{ V}$ .  $V_{\text{in}}$ , input voltage.

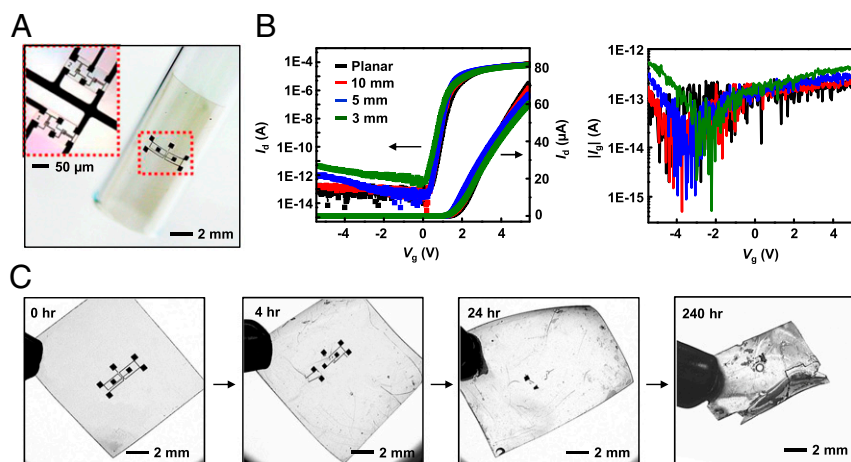


**Fig. 5.** Foundry-based transient electronic systems on a PLGA substrate. (A) Optical micrographs of transient logic gates (similar to the transient logic gates shown in Fig. 3) on a thin film of PLGA wrapped onto a glass cylinder. (Inset) Magnified view of the interconnected MOSFETs. (B) Current-voltage characteristics of typical n-channel MOSFETs mounted on cylinders with different diameters.  $I_g$ , gate leakage current. (C) Optical micrographs at various stages of dissolution and disintegration of transient electronics that integrate foundry-based microelectronics on the thin PLGA sheet. This accelerated dissolution test is performed in an aqueous buffer solution (pH 7.4) at 70 °C.

with this mechanism and with data on related devices reported elsewhere (43, 44).

The entire systems dissolve in water, beginning with the PLGA. A sequence of images captured during dissolution in PBS (pH 7.4) at 70 °C appears in Fig. 5C. In this example, hydrolytic degradation of the PLGA leads to swelling and buckling processes that cause fracture and disintegration of the W traces within 24 h. The PLGA loses its mechanical strength via random chemical scission of the ester backbone and resulting changes in morphology, pH, and crystalline properties, resulting in the degradation or failure of the interconnected system at this stage (45, 46). By comparison, the device blocks dissolve much more slowly, in a manner determined by the constituent materials and their corresponding structures as described in detail subsequently. Timescales for complete dissolution of the PLGA sheets ( $\approx 20 \mu\text{m}$ ) are  $\sim 15\text{--}20$  d, as determined by the chemical composition and molecular weight.

Accelerated tests (immersion in PBS at 96 °C) provide information on the kinetics of dissolution of the devices themselves. Fig. 6A presents a series of optical images collected during dissolution of an array of devices similar in materials and layout to the components in Fig. 1. In this example, apparent physical changes in device morphology imply material decomposition as a result of soaking. The changes initiate at structural edges, followed in other regions by successive downward etching, on a layer-by-layer basis. Extrinsic material properties, such as porosity, pitting, or other nonuniformities, can influence the process. Additional details obtained by measuring thicknesses as a function of time further establish the kinetics of hydrolysis of W, PECVD  $\text{SiN}_x$ , PECVD  $\text{SiO}_2$ , and thermal  $\text{SiO}_2$ . The data appear in Fig. 6B, where the morphological thicknesses correspond to physical changes measured directly by profilometry and the effective thicknesses correspond to approximate changes derived from measured sheet resistances,  $R_s$ , according to  $R_s = \rho/t$  (with constant resistivity  $\rho$  and an initial thickness of 300 nm). Corresponding stages of dissolution in physical transience are shown in Fig. 6C. Hydrolysis consumes  $\text{SiN}_x$  in a uniform fashion at a rate of  $\sim 0.2 \mu\text{m}\cdot\text{d}^{-1}$  according to  $\text{Si}_3\text{N}_4 + 6\text{H}_2\text{O} \rightarrow 3\text{SiO}_2 + 4\text{NH}_3$ , followed by the dissolution of the PECVD  $\text{SiO}_2$  interlayer [ $\text{SiO}_2 + 2\text{H}_2\text{O} \rightarrow \text{Si}(\text{OH})_4$ ] at a rate of  $\sim 0.7 \mu\text{m}\cdot\text{d}^{-1}$ ; in the meantime, W interconnects ( $2\text{W} + 2\text{H}_2\text{O} + 3\text{O}_2 \rightarrow 2\text{H}_2\text{WO}_4$ ) and Si layers dissolve [ $\text{Si} + 4\text{H}_2\text{O} \rightarrow \text{Si}(\text{OH})_4 + 2\text{H}_2$ ] on timescales of 24 h. After the layered structure mostly disappears, the underlying BOX (thermally grown  $\text{SiO}_2$ ) dissolves

over the following 10 d, thereby establishing the overall timescale for transience. These results are consistent with previous reports of dissolution kinetics for nonfoundry silicon-based transient electronics (21, 47–49).

Corresponding changes in microstructure during dissolution of a single device can be studied via cross-sectional SEM, as shown in Fig. 7. The schematic illustration provides information on the structure and material constituents: PECVD  $\text{SiO}_2$  for IMD ( $\approx 650$  nm) and ILD ( $\approx 750$  nm) layers, W ( $\approx 300$  nm) for metal interconnects, Ti/TiN ( $\approx 100$  nm) for the adhesion promoter, thermal  $\text{SiO}_2$  ( $\approx 1 \mu\text{m}$ ) BOX, and device Si ( $\approx 250$  nm), including the polycrystalline silicon gate ( $\approx 80$  nm), doped silicon, and  $\text{SiO}_2$  gate dielectric ( $\approx 25$  nm). Each component, except the Ti/TiN adhesive layer, dissolves in a manner determined by the corresponding hydrolysis rates of the materials, the presence and type of morphological defects (e.g., pores/pinholes/microcracks), and the characteristics of the surrounding solution (pH, temperature, agitation/convection). The first stage corresponds to disintegration of the IMD and ILD layers and the W interconnects, beginning with the exposed W at the contact pads. Reactive dissolution that undercuts the embedded W lines exfoliates the layered structure due to permeation of the PBS, followed by delamination of the Ti/TiN layer. This type of disintegration occurs mostly due to delamination, peeling, and formation of flakes. Although Ti undergoes oxidation ( $\text{Ti} + 2\text{H}_2\text{O} \rightarrow \text{TiO}_2 + 2\text{H}_2$ ), further chemical reactions are typically terminated by the oxide product (50). Hence, the Ti/TiN layer tends to peel off after disintegration of the supporting ILD layer during this dissolution stage. The second stage involves dissolution of the active Si, starting along structural relief in a fashion that depends on the presence of residual ILD material (etching barriers or natural microvoids from local defects). Finally, the thermal  $\text{SiO}_2$  slowly dissolves during the last stage, typically in a spatially uniform fashion across the entire area. As shown in the SEM images, PBS soaking tests leave patterns on the BOX layer with the lateral dimensions of devices. Immersion for  $\sim 2$  wk leads to complete dissolution under these conditions; at 5 d, everything except the BOX is eliminated. Clearly, a decrease in the BOX thickness will reduce the overall dissolution time (e.g., foundry-based transient electronics with 100-nm-thick BOX layer are projected to dissolve within a week under these conditions).



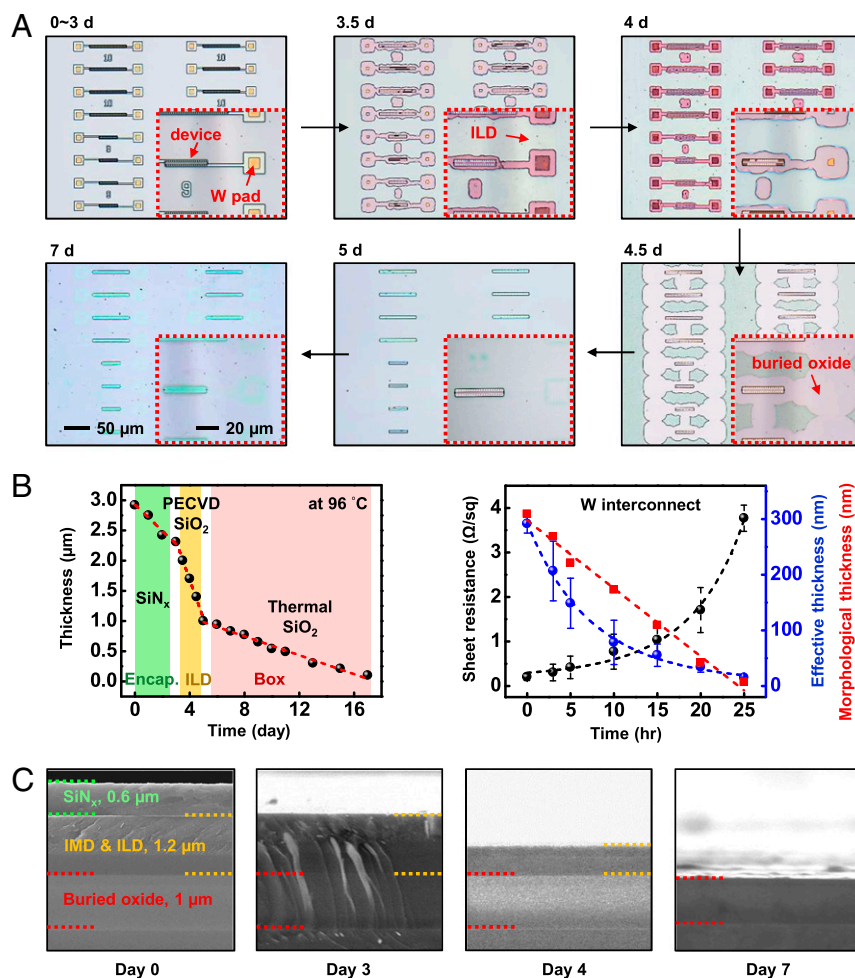


**Fig. 6.** Evolution of device structures and material layers in transient electronic devices during dissolution. (A) Optical images of arrays of devices during accelerated dissolution upon immersion in an aqueous buffer solution (pH 7.4) at 96 °C. The device structures include  $\text{SiN}_x$  encapsulation ( $\approx 600$  nm), W interconnects ( $\approx 300$  nm), PECVD  $\text{SiO}_2$  interlayers ( $\approx 1.2$   $\mu\text{m}$ ), and Si active layers ( $\approx 250$  nm), with an underlying layer of  $\text{SiO}_2$  ( $\approx 1$   $\mu\text{m}$ ; BOX). (B) Time evolution of device thickness associated with different constituent materials during the dissolution test. The estimated dissolution rates are  $\sim 0.2$   $\mu\text{m}\cdot\text{d}^{-1}$  for PECVD  $\text{SiN}_x$ ,  $\sim 0.7$   $\mu\text{m}\cdot\text{d}^{-1}$  for PECVD  $\text{SiO}_2$ ,  $< 0.1$   $\mu\text{m}\cdot\text{d}^{-1}$  for thermal  $\text{SiO}_2$ , and  $\sim 0.3$   $\mu\text{m}\cdot\text{d}^{-1}$  for W. (C) Cross-sectional SEM images collected at several stages of device dissolution. The decreases in device thickness account for the dissolution rate and data in B. The SEM images were taken at 13,000 $\times$  magnification.

## Conclusion

The materials, fabrication strategies, and integration schemes reported here enable the use of foundry-compatible, full-wafer processing capabilities in transient electronics. Microscale assembly of state-of-art CMOS devices onto soft materials avoids constraints in materials choices that would otherwise follow from foundry-standard manufacturing temperatures, processing solvents, and other conditions that are incompatible with bioresorbable polymers. Anisotropic etching as a release strategy and selective transfer printing as a means for device manipulation provide versatility in forming functional systems with wide-ranging application possibilities. The outcomes could qualitatively extend conventional foundry-based manufacturing capacity and affiliated supporting infrastructure in circuit and device design to nearly all envisioned applications in transient electronics. These findings enable the translation of modern chip technologies into environmentally friendly, biodegradable systems.

## Materials and Methods

**Fabrication of Foundry-Based Transient Logic Gates.** Fully formed microelectronics fabricated on 6-inch SOI (100) wafers with active layers of Si ( $\approx 250$  nm), gate oxide ( $\approx 25$  nm), ILD ( $\approx 750$  nm) and IMD ( $\approx 650$  nm) layers, Ti/TiN ( $\approx 100$  nm), and W interconnects ( $\approx 300$  nm) as the source of transient active

devices. The Ti/TiN layer at the via plugs, which comprises less than 1% of the overall area of a typical device and less than 0.05% of its overall mass, is the only component that is not water-soluble. Photolithography and ICP-RIE (STS Mesc Multiplex) with  $\text{SF}_6$  yielded isolated device blocks. This ICP-RIE step formed trenches to the underlying Si (100) handle wafer through the IMD, ILD, and BOX layers. A 600-nm-thick, low-stress  $\text{SiN}_x$  layer deposited by PECVD (STS Mesc Multiplex tool; mixed frequency RF power of 20 W) served as the material for the anchors and etching barriers. An additional ICP-RIE step defined the former so as to tether the device blocks to their lithographically defined locations and to prevent them from washing away during the undercut etching process. This etching involved complete immersion in a static solution of 8.3% TMAH (at 85 °C) or 18% KOH (at 70 °C). Devices released in this way exist in a freely suspended configuration, suitable for transfer printing from the source wafer onto a target substrate. To facilitate this transfer process, a thin sheet of PLGA (Sigma-Aldrich) annealed at temperatures near the glass transition of the PLGA (65 °C; molecular weight of 50,000–75,000) served as the receiving substrate. A spin-cast layer of PLGA (85:15; 2  $\mu\text{m}$  thick) planarized the resulting platform, following transfer. A thin film of Mg (100 nm) deposited by sputtering and patterned by photolithography and etching provided a hard mask for etching through the PLGA by RIE to expose the contact pads of the underlying device blocks. Removal of the Mg, followed by patterning of the sputtered layer of W (300 nm) by photolithography and etching, completed the fabrication.

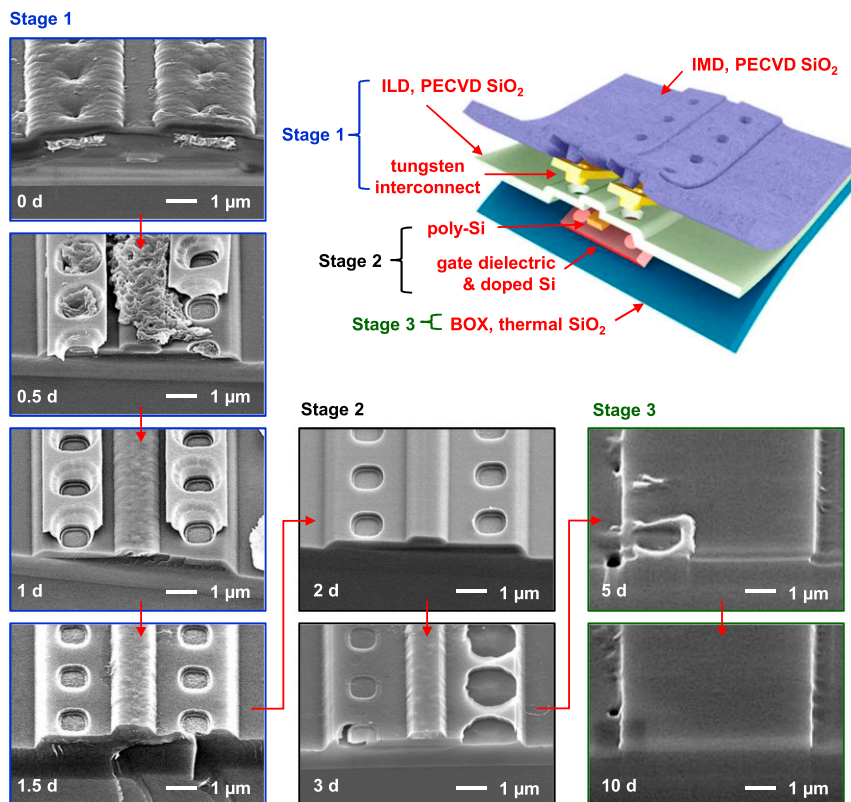


**Fig. 7.** Disintegration of layered microstructures in a transient electronic device during dissolution. A schematic illustration and a time sequence of SEM images of disintegration of foundry-based transient microelectronic devices are shown. The device structure and test conditions for the dissolution test are the same as in Fig. 6.

**Dissolution Testing.** A transparent PDMS enclosure bonded to the surface of a processed wafer confined a volume of PBS (pH 7.4; Sigma–Aldrich) for dissolution testing in a manner that allowed for in situ observation with an optical microscope. A programmable hotplate controlled the temperature. The PBS solutions were replaced every other day during the course of dissolution. For ex situ characterization (Hitachi S4800 SEM system or FEI DB235 focus ion beam system), the samples were removed from the enclosure and gently rinsed with deionized water. Electrical characterization was performed with a semiconductor parameter analyzer (4155C; Agilent) and a probe station in a dark box. Measurements of the W interconnection involved a cylindrical four-point probe setup (Jandel) to determine the sheet resistance

(and, with appropriate calibration, the thickness) and a profilometer (Dektak) and/or atomic force microscope (MFP-3D; Asylum Research) to determine the thicknesses.

**ACKNOWLEDGMENTS.** We thank the Micro and Nanotechnology Laboratory and the Micro-Nano-Mechanical Systems Laboratory at the University of Illinois at Urbana–Champaign for device fabrication and material characterization. We thank Dr. Dan Harburg for informative discussions. This work was supported by the Center for Bio-Integrated Electronics at Northwestern University. J.-K.C. received support from Ministry of Science and Technology, Taiwan (Project 105-2917-I-564-038).

- Venema L (2011) Silicon electronics and beyond. *Nature* 479:309.
- Bagley B (2016) Semiconductor financing: Recent trends. *2016 28th International Symposium on Power Semiconductor Devices and ICs (ISPSD)* (IEEE, Prague, Czech Republic), pp 1–4.
- Zhu Y, Xiong J (2015) Modern big data analytics for old-fashioned semiconductor industry applications. *Proceedings of the IEEE/ACM International Conference on Computer-Aided Design* (IEEE Press, Piscataway, NJ), pp 776–780.
- World Semiconductor Trade Statistics (2017) WSTS Semiconductor Market Forecast Spring 2017. WSTS Forecasts the Semiconductor Market's Largest Growth Year in More Than Five Years. Available at: <https://www.wsts.org/PRESS/Recent-News-Release>. Accessed March 28, 2017.
- Lorenzen JA (2014) Green consumption and social change: Debates over responsibility, private action, and access. *Social Compass* 8:1063–1081.
- Tanskanen P (2013) Management and recycling of electronic waste. *Acta Mater* 61: 1001–1011.
- Fang S, et al. (2014) An integrated system for regional environmental monitoring and management based on internet of things. *IEEE Trans Industr Inform* 10:1596–1605.
- Da Xu L, He W, Li S (2014) Internet of things in industries: A survey. *IEEE Trans Industr Inform* 10:2233–2243.
- Zhou Y, et al. (2014) Efficient recyclable organic solar cells on cellulose nanocrystal substrates with a conducting polymer top electrode deposited by film-transfer lamination. *Org Electron* 15:661–666.
- Kang SK, et al. (2016) Bioresorbable silicon electronic sensors for the brain. *Nature* 530:71–76.
- Jung YH, et al. (2015) High-performance green flexible electronics based on biodegradable cellulose nanofibril paper. *Nat Commun* 6:7170.
- Huang X, et al. (2014) Biodegradable materials for multilayer transient printed circuit boards. *Adv Mater* 26:7371–7377.
- Kim BH, et al. (2017) Dry transient electronic systems by use of materials that sublime. *Adv Funct Mater* 27:1606008.
- Bettinger CJ, Bao Z (2010) Organic thin-film transistors fabricated on resorbable biomaterial substrates. *Adv Mater* 22:651–655.
- Irimia-Vladu M (2014) "Green" electronics: Biodegradable and biocompatible materials and devices for sustainable future. *Chem Soc Rev* 43:588–610.
- Muskovich M, Bettinger CJ (2012) Biomaterials-based electronics: Polymers and interfaces for biology and medicine. *Adv Healthc Mater* 1:248–266.
- Hwang SW, et al. (2015) Materials for programmed, functional transformation in transient electronic systems. *Adv Mater* 27:47–52.
- Hwang SW, et al. (2012) A physically transient form of silicon electronics. *Science* 337: 1640–1644.
- Hwang SW, et al. (2014) High-performance biodegradable/transient electronics on biodegradable polymers. *Adv Mater* 26:3905–3911.
- Kang SK, et al. (2015) Biodegradable thin metal foils and spin-on glass materials for transient electronics. *Adv Funct Mater* 25:1789–1797.
- Kang SK, et al. (2014) Dissolution behaviors and applications of silicon oxides and nitrides in transient electronics. *Adv Funct Mater* 24:4427–4434.
- Yin L, et al. (2014) Dissolvable metals for transient electronics. *Adv Funct Mater* 24: 645–658.
- Kang SK, et al. (2015) Dissolution chemistry and biocompatibility of silicon- and germanium-based semiconductors for transient electronics. *ACS Appl Mater Interfaces* 7:9297–9305.

24. Yu KJ, et al. (2016) Bioresorbable silicon electronics for transient spatiotemporal mapping of electrical activity from the cerebral cortex. *Nat Mater* 15:782–791.
25. Fu K, et al. (2015) Transient rechargeable batteries triggered by cascade reactions. *Nano Lett* 15:4664–4671.
26. Hwang SW, et al. (2015) Biodegradable elastomers and silicon nanomembranes/nanoribbons for stretchable, transient electronics, and biosensors. *Nano Lett* 15: 2801–2808.
27. Hwang SW, et al. (2013) Materials for bioresorbable radio frequency electronics. *Adv Mater* 25:3526–3531.
28. Edupuganti V, Solanki R (2016) Fabrication, characterization, and modeling of a biodegradable battery for transient electronics. *J Power Sources* 336:447–454.
29. Fu KK, et al. (2016) Transient electronics: Materials and devices. *Chem Mater* 28: 3527–3539.
30. Chen Y, et al. (2015) Characterizing physically transient antennas. *IEEE Trans Antennas Propag* 63:2421–2429.
31. Patrick E, Orazem ME, Sanchez JC, Nishida T (2011) Corrosion of tungsten micro-electrodes used in neural recording applications. *J Neurosci Meth* 198:158–171.
32. Chen Q, Thouas GA (2015) Metallic implant biomaterials. *Mater Sci Eng R-Rep* 87: 1–57.
33. Kim DH, et al. (2008) Complementary logic gates and ring oscillators on plastic substrates by use of printed ribbons of single-crystalline silicon. *IEEE Electron Device Lett* 29:73–76.
34. Baca AJ, et al. (2007) Printable single-crystal silicon micro/nanoscale ribbons, platelets and bars generated from bulk wafers. *Adv Funct Mater* 17:3051–3062.
35. Sun L, et al. (2010) 12-GHz thin-film transistors on transferrable silicon nanomembranes for high-performance flexible electronics. *Small* 6:2553–2557.
36. Yin L, et al. (2015) Materials and fabrication sequences for water soluble silicon integrated circuits at the 90 nm node. *Appl Phys Lett* 106:014105.
37. Riches S, Johnston C (2015) Electronics design, assembly and reliability for high temperature applications. *2015 IEEE International Symposium on Circuits and Systems* (IEEE, Lisbon, Portugal), pp 1158–1161.
38. Paun MA, Udrea F (2016) Investigation into the capabilities of Hall cells integrated in a non-fully depleted SOI CMOS technological process. *Sens Actuators A Phys* 242:43–49.
39. Landsberger LM, Naseh S, Kahrizi M, Paranjape M (1996) On hillocks generated during anisotropic etching of Si in TMAH. *J Microelectromech Syst* 5:106–116.
40. Carlson A, Bowen AM, Huang Y, Nuzzo RG, Rogers JA (2012) Transfer printing techniques for materials assembly and micro/nanodevice fabrication. *Adv Mater* 24:5284–5318.
41. Sun Y, Thompson SE, Nishida T (2007) Physics of strain effects in semiconductors and metal-oxide-semiconductor field-effect transistors. *J Appl Phys* 101:104503.
42. Gamiz F, Cartujo-Cassinello P, Roldán JB, Jiménez-Molinos F (2002) Electron transport in strained Si inversion layers grown on SiGe-on-insulator substrates. *J Appl Phys* 92: 288–295.
43. Kim HS, et al. (2009) Self-assembled nanodielectrics and silicon nanomembranes for low voltage, flexible transistors, and logic gates on plastic substrates. *Appl Phys Lett* 95:183504.
44. Zhao W, He J, Belford RE, Wernersson LE, Seabaugh A (2004) Partially depleted SOI MOSFETs under uniaxial tensile strain. *IEEE Trans Electron Dev* 51:317–323.
45. Göpferich A (1996) Mechanisms of polymer degradation and erosion. *Biomaterials* 17: 103–114.
46. Athanasiou KA, Niederauer GG, Agrawal CM (1996) Sterilization, toxicity, biocompatibility and clinical applications of polylactic acid/polyglycolic acid copolymers. *Biomaterials* 17:93–102.
47. Hwang SW, et al. (2013) Materials and fabrication processes for transient and bioresorbable high-performance electronics. *Adv Funct Mater* 23:4087–4093.
48. Fang H, et al. (2016) Ultrathin, transferred layers of thermally grown silicon dioxide as biofluid barriers for biointegrated flexible electronic systems. *Proc Natl Acad Sci USA* 113:11682–11687.
49. Hwang SW, et al. (2014) Dissolution chemistry and biocompatibility of single-crystalline silicon nanomembranes and associated materials for transient electronics. *ACS Nano* 8: 5843–5851.
50. Oshida Y (2010) *Bioscience and Bioengineering of Titanium Materials* (Elsevier, London).